# Designing nanomechanical resonators for high-frequency gravitational wave detection

Juan P.A. Maldonado, University of Bonn, Germany

DESY Summer Student Program 2022

Supervised by: Dr. Christoph Reinhardt
Dr. Udai Singh
Dr. Axel Lindner

ALPS research group at DESY

September 7, 2022

## Abstract

Fueled by recent achievements of km-scale gravitational-wave interferometers, the development of ”smaller-scale” detectors are currently gaining momentum. By virtue of their smaller dimensions, these detectors target gravitational-waves at frequencies above the established observation window (i.e., 10 to $10^4$ Hz). A particular example is the levitated sensor detector, currently under development at Northwestern University, which targets gravitational waves in the range of $10^4$ to $10^6$ Hz. The setup comprises a nanoparticle, which is optically levitated at the anti-node of a standing wave formed by a laser inside an optical cavity. Upon passing of a gravitational wave the particle is displaced from its equilibrium position, which is recorded with a second laser beam. As an alternative to using a levitated nanoparticle we consider a ”partially-levitated” membrane. In order to realize sensitivities compatible with the levitated sensor detector, a nanomechanical membrane resonator with ultra-high-quality factor is required, to suppress the impact from thermal noise. In the present project, we show, by means of simulations in COMSOL Multiphysics, that tenfold increasing the lateral extent of a state-of-the-art membrane resonator enables a hundredfold increase of its quality factor. This provides a possible route towards realizing membrane resonators for high-frequency (e.g., $\sim 100$ kHz) gravitational-wave detection. To further increase the Q factor and suppress the impact from thermal noise, we consider cooling the membrane with a continuous-flow cryostat. As a first step towards estimating the corresponding helium consumption, we investigate a related analytical model.

# Contents

# 1. Introduction

## 1.1. Detecting the axion with Gravitational Waves

One of the most well-motivated dark matter candidates is the QCD-axion. First proposed as an explanation of the strong CP problem [1], its discovery would represent a major breakthrough in the understanding of the universe, as it has great impact both in particle physics and cosmology. Experiments sensitive to this particle in different regions of the parameter space include MADMAX [2] and IAXO [3].

If the mass of the QCD axion lies in the interval of $10^{-22}\,\mathrm{eV} \leq m_a \leq 10^{-10}\,\mathrm{eV}$, it could affect the dynamics and GW emission of rapidly rotatig astrophysical black holes thorugh the Penrose superradiance process [4]. In this mass range, the Compton wavelength of a bosonic dark matter particle is comparable to the size of stellar mass black holes, thus creating a gravitational atom that can be excited due to the high angular momentum of the rotatig black hole. This excited state can go through de-excitation by emitting GWs with frequencies in the order of $10^5\,\mathrm{Hz}$. At frequencies beyond 10 kHz there is a lack of known astrophysical objects which are small and dense enough to emit GWs efficiently, which significantly reduces the noise that is usually obtained when probing an exotic particle by dominant processes which produce similar signals.

GW detectors like LIGO [5] have already been commissioned and succesfully detected GWs from violent processes such as the merger of black holes [6]. Improved GW interferometers like LISA [7] and the Einstein Telescope [8] are also subject of research and are planned to start operation in the next decades. However, the sensitivity of GW interferometers excel at low-frequency detection but is strongly supressed in the high-frequency ($\gtrsim 10^4\,\mathrm{Hz}$) mainly because of laser shot noise and the smaller signal at shorter wavelengths.
For this reason, novel techniques for high-frequency GW detection are relevant and can have an enormous impact in fundamental research [9]. A particular example of a high-frequency gravitational wave detector is the levitated sensor detector [10, 11]. Here, a dielectric nano-particle is optically-trapped at the anti-node of the laser's standing wave inside an optical cavity. A passing gravitational wave causes a time-varying strain of the physical length of the cavity. This causes the nanoparticle to oscillate around its equilibrium position, if the optical trapping frequency (widely tunable via the optical power) agrees with the frequency of the gravitational wave. The resulting oscillation is read out with an additional optical probe beam [12]. As an alternative approach to using a levitated nano-particle, we consider a partially-levitated membrane [13]. Here, the mechanical restoring force, acting on the membrane up on displacement from its equilibrium position, is a superposition of the optical restoring force and the membrane's elasticity. To achieve a high signal to noise ratio (SNR), a large mechanical quality factor is required, as it suppresses the impact from thermal noise.

## 1.2. Ultra-coherent nano-mechanical membrane resonators

Nanomechanical resonators are chip-scale implementations of a harmonic oscillator. They have a wide range of applications in sensing and cavity optomechanics [14].
The Q factor parametrizes how fast is the energy stored in an oscillator dissipated. Reducing force noise ($\propto Q^{-1/2}$) or decoherence rate ($\propto Q^{-1}$) have been major drivers in creating nano-mechanical resonators with ultra-high Q. A specific class of nano-mechanical resonators with ultra-high-Q are made out of strained thin films with high tensile stress $\sigma \sim$ 1GPa [15]. Promising ways for further improving high Q-factor membrane resonators include material research and geometry optimization. Regarding the former aspect, $Si_3N_4$ was selected for this study because it has emerged as a powerful mechanical resonator material, featuring some of the highest Q-factors ever achieved [16]. These resonators show even at room temperature $\sim$ MHz resonances with sub-Hz damping rates (equivalent to $Q \sim 10^9$ [17]. The present work focuses on the enhancement in the Q-factor by ncreasing the lateral extent of a thin-film membrane resonator, which is investigated by simulating expected Q factors in COMSOL Multiphysics [18].

The mechanical quality factor $Q$ of a membrane resonator is defined as

$$Q = 2\pi \times \frac{K}{\Delta K} \tag{1.1}$$

where $K$ represents the energy stored in the oscillator and $\Delta K$ the energy lost per cycle of oscillation. To compute this quantity in the simulated resonators, the total energy stored is calcualted as [19]

$$K = 2\pi^2 f^2 \rho h \iint_S z(x,y)^2 dS, \tag{1.2}$$

where $f$ is the resonance frequency, $\rho$ the density of the material, $h$ its thickness, and $z$ the amplitude of vibration perpendicular to the membrane. The integral is evaluated over the surface of the resonator. Note that this definition can be interpreted as the superposition of the total energy stored for a large number of infinitesimal resonators.
Analogously, the energy lost per oscillation cycle can be defined as

$$\Delta K = \pi Y h^3 \frac{\phi}{12(1-\nu^2)} \iint_S \left(\frac{\partial^2 z}{\partial x^2} + \frac{\partial^2 z}{\partial y^2}\right)^2 - 2(1-\nu)\left[\frac{\partial^2 z}{\partial x^2}\frac{\partial^2 z}{\partial y^2} - \left(\frac{\partial^2 z}{\partial x \partial y}\right)^2\right] dS \tag{1.3}$$

Where $Y$ is the Young modulus, $\nu$ the Poisson ratio, and $\phi$ the local loss angle distribution defined as

$$\phi = \frac{1}{\beta h} \tag{1.4}$$

with $\beta$ represents the inverse loss angle coefficient. There are equivalent definitions that use, for example, the complex and real components of a Young modulus instead of its norm and the local loss angle distribution. However, for the purposes of these work, the variables here introduced were the parameters used to model a specific material in the simulations

# 2. Simulations

The following simulations or some parts of it were run on a local computer [1] and on the Maxwell cluster, mainly for parallel computations between different models. The reported computation times are given in terms of the local machine specifications.

## 2.1. Square membrane

A straightforward way to start is by comparing the quantities computed numerically by COMSOL to a well-known analytical case. Specifically, a square membrane of side $L$ is simulated implementing Cauchy conditions on its edges. This simple model has eigenfrequencies that can be computed analitically by means of equation 2.1 [15].

$$f_{m,n} = \frac{1}{2L}\sqrt{\frac{\sigma}{\rho}(m^2 + n^2)}. \tag{2.1}$$

Where $f_{m,n}$ denotes the frequency mode (note that there are degenerated modes for $m = n$), $\sigma$ is the in-plane tensile stress and $\rho$ the density of the material. The numerical values used to characterize the membrane are as follows:

- Young modulus $Y = 250\,\mathrm{GPa}$
- Lateral extent $L = 500\mu\mathrm{m}$
- Thickness $100\,\mathrm{nm}$
- Poisson ratio $\nu = 0.23$
- Density $\rho = 2700\,\mathrm{kgm}^{-3}$
- Stress $\sigma = 1\,\mathrm{GPa}$
- Inverse loss angle coefficient $\Phi = 3.14 \times 10^{-5}$

The simulation first does a stationary step to redistribute the loads (i.e. the tensile stress) on the membrane and finds numerically the eigenfrequencies and corresponding mode shapes of oscillation. To do this, a mesh is created to do the finite element simulation. Figure 1 shows the distribution of the mesh elements.

[1] Intel core i5-8350, 16 GB RAM, 120 free GB of SSD

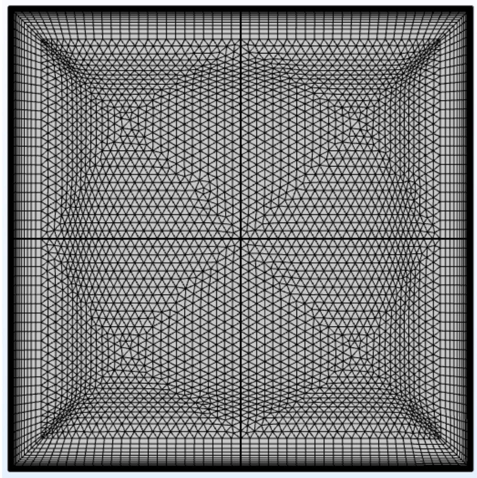

Figure 1: Mesh elements for the square membrane simulation.

Note that the elements decrease in size when approaching the edges of the membrane, this is required to compute an accurate Q factor, because this region will feature high energy loss, as seen in figure 3. The modes corresponding to the first eigenfrequencies, computed in the second step of the simulation, are also shown in figure 2.

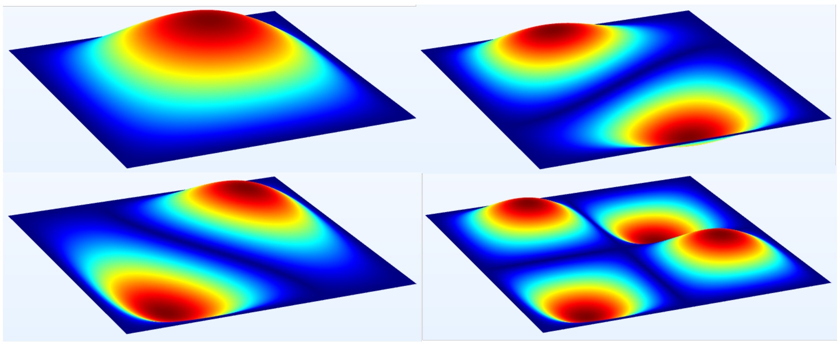

Figure 2: Visualization of modes for the first four eigenfrequencies. The upper-left corresponding to the fundamental mode of this membrane.

The numerical values for these eigenfrequencies are displayed in Table 1, along with the analytical solution obtained using equation 2.1.

| (n,m) | Analytical (kHz) | Numerical (kHz) | Error % |
|---|---|---|---|
| (1,1) | 860.66 | 862.28 | 0.19 |
| (1,2),(2,1) | 1360.8 | 1363.4 | 0.19 |
| (2,2) | 1721.3 | 1724.6 | 0.19 |

Table 1: First four eigenfrequencies for a simple square membrane model

The eigenfrequencies found numerically match those calculated analytically to high precision, with a default mesh for *general physics* and element size set to *fine*.

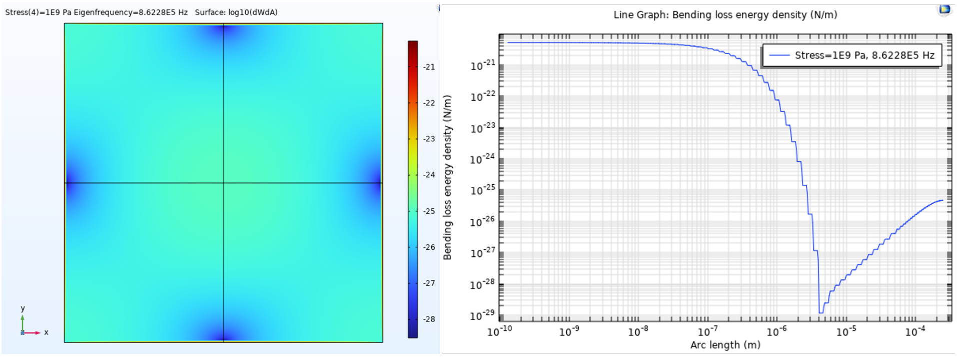


Figure 3: Energy loss density (log scale) due to the bending of the square membrane. Note that approaching the edge, the loss increases by several orders of magnitude

It is also useful to study the energy loss density in this model, to estimate where most of the energy loss is happening, thus determining the Q factor achievable with this particular device. As seen in figure 3, the edges of the membrane is the predominant area where energy is lost, due to the fixed clamping (i.e. Cauchy boundary conditions) that holds the membrane. The effect of energy loss at the clamping edges of a fixed membrane has been largely studied and reported [20, 21]. To attain larger Q factors, different geometries have been proposed such that this effect can be avoided (see, e.g. [22]). Notably, The possibility of modifying the square membrane introducing a semi-periodic hexagonal lattice [23] has proven to be a promising alternative to achieve larger Q factors, which could enable, among many applications, to measuring high-frequency gravitational waves [11].

## 2.2. Phononic crystal

One way to address the problem of high energy loss on the clamped edges of a square membrane is proposed by [23]. A central defect enables a set of localized modes, which strongly suppress displacement and correspnding bending-related losses at the clamps. The figure 4 shows the first defect mode. By virtue of its symmetry it couples to an incident laser beam (shown in red), via the radiation pressure force. Installing such a membrane inside an optical cavity, such as used in the ALPS-II experiment, thereby coupling it to the intra-cavity field, might enable the detection of gravitational waves [11]. As a first step, towards adapting the design of the phononic crystal membrane for gravitational wave detection, we implement a corresponding COMSOL model for resonance frequencies and quality factors, which we validate with regard to the results presented in [23].
To study the phononic crystal behaviour, a 3D shell is simulated in COMSOL [18], by implementing a stationary step to redistribute the loads and a subsequent eigenfrequency step.

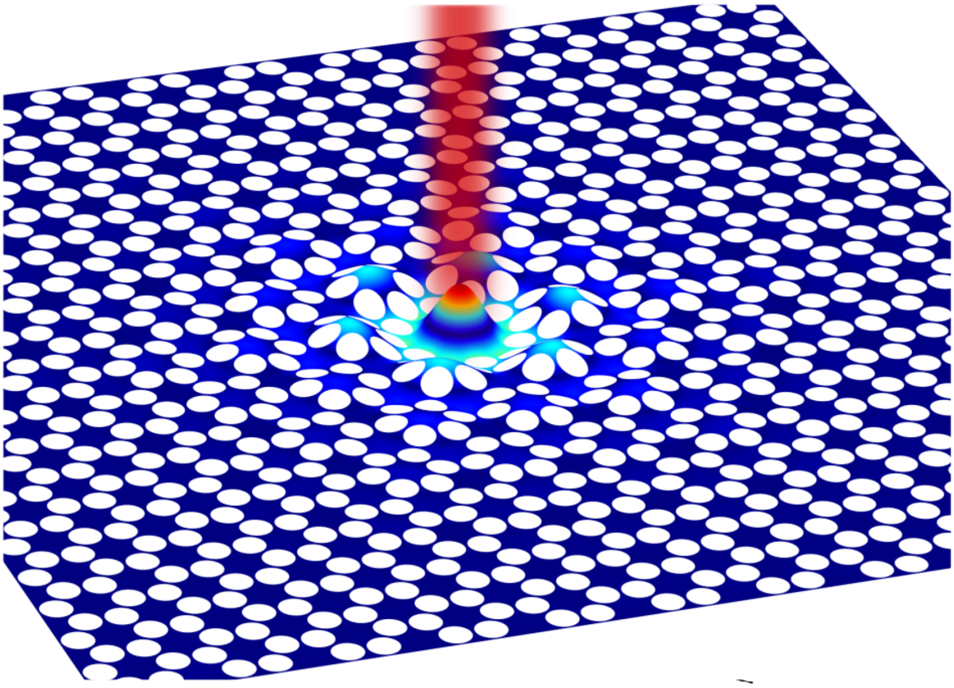

Figure 4: Advantageous shape of the fundamental defect mode when coupling to an incident laser beam

#### 2.2.1. Material properties

The material properties were chosen in accordance to [23]. Table 2 show the input parameters of the simulation, formulated consistently to use the equations introduced in section 1.

| Name | Value | Comment |
|---|---|---|
| $\sigma$ | 1.27 GPa | In-plane stress |
| $\rho$ | $3.20\ \frac{\mathrm{g}}{\mathrm{cm}^3}$ | Material density |
| $E_1$ | 270 GPa | Real part of Young's modulus |
| $\nu$ | 0.27 | Poisson ratio |
| $\beta$ | $2.93 \times 10^{11}\ \mathrm{m}^{-1}$ | Inverse loss angle coefficient |

Table 2: Material characterization for the membrane

Where $E_1, \beta = E_2/E_1$ is an alternative way to describe the Young modulus $Y = E_1 + \imath E_2$, which expresses the relation between the stress and the strain on the material. $\sigma$ quantifies the tensile stress in the membrane. Complementary, the strain describes the amount of deformation of a body caused by a tensile stress, relative to its natural size. Finally, the Poisson ratio expresses the deformation on an orthogonal axis to the direction of applied stress. For the case of the membrane, it quantifies the deformation on the z-axis, i.e. the oscillation direction, caused by the in-plane stress. In the range of $0 < \nu < 0.5$, an in-plane stress greater than 0 (tensile stress) will cause the compresion

of the body in the orthogonal direction.
The values here used are typical for a silicon nitride $Si_3N_4$ membrane, and match exactly those measured and reported in [23].

### 2.2.2. Geometry

A thin semi-periodic phononic crystal is simulated using the parameters shown in table 3. These parameters are chosen to match those reported [23] in order to validate the model.

| Name | Value | Comment |
|---|---|---|
| a | 0.160 (mm) | Lattice constant |
| $h$ | 35 (nm) | Thickness |
| r | $0.26 \times a$ | Radius of membrane holes |
| $\nu$ | 0.27 | Poisson ratio |
| $\beta$ | $2.93 \times 10^{11}\,\mathrm{m}^{-1}$ | Inverse loss angle coefficient |

Table 3: Geometry of the membrane. The value for $\beta$ was taken from [24]

Figure 5 shows the dimensions of the unit cell used for the creation of the periodic component of the membrane array, based on the unit vectors of a hexagonal unit cell.

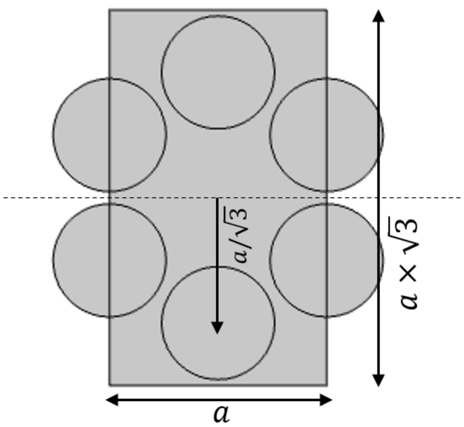


Figure 5: Unit cell of the membrane before computing the difference of the rectangle and the six circles

where $a$ denotes the lattice constant. Then, as shown in figure 6, the geometry of the full membrane can be created by joining multiple unit cells and creating a central defect of a size similar to $a$. Finally, a central bigger circle is appended to simulate the illuminated region by the probe laser for measuring the membrane's oscillation of the sensing laser. The radius was chosen to cover completely the central defect and the expected zone around it with high oscillation amplitude.

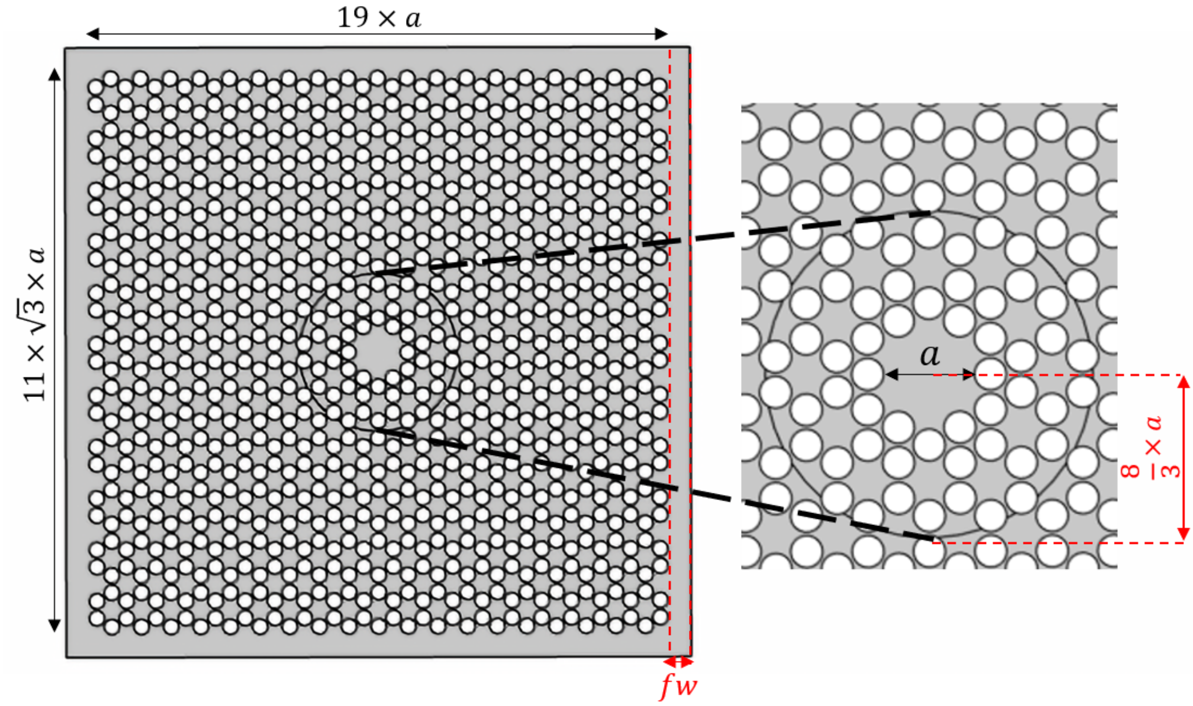


Figure 6: Complete membrane geometry included the scanning region of the sensing laser around the central defect.

To reduce possible redundant vertices or edges the built-in function *Remove details* was selected. Eliminating these redundancies is a good practice to avoid not optimal meshing, though for the case of study there was no impact.
When completing the full geometry, a total of 1736 edges and 1718 vertices are created.

### 2.2.3. Mesh elements

To construct the mesh, the *extremely fine* mesh elements of a free triangular mesh are further varied until the size at the defect looks fine enough. To check that the selected values are small enough, the plots obtained during the analysis step are checked, where it is expected to see smooth behaviours in the graphs. Moreover, in section 2.3 a complementary sanity check is explained. Figure 7 shows how the final meshing looks like near the edge of the membrane and in the region of the defect mode. The creation of the mesh outputs a total of $1.55 \times 10^6$ degrees of freedom. Care must be taken not to use an overly-fine mesh as it can have a drastic impact on the memory and computation time[1], without any measurable change in the computed quantities.

### 2.2.4. Defect modes

The simulation computed the first 600 eigenfrequencies and its mode profiles. By scanning the movement around the central defect using the central circle it is possible to

[1]https://www.comsol.com/support/knowledgebase/875

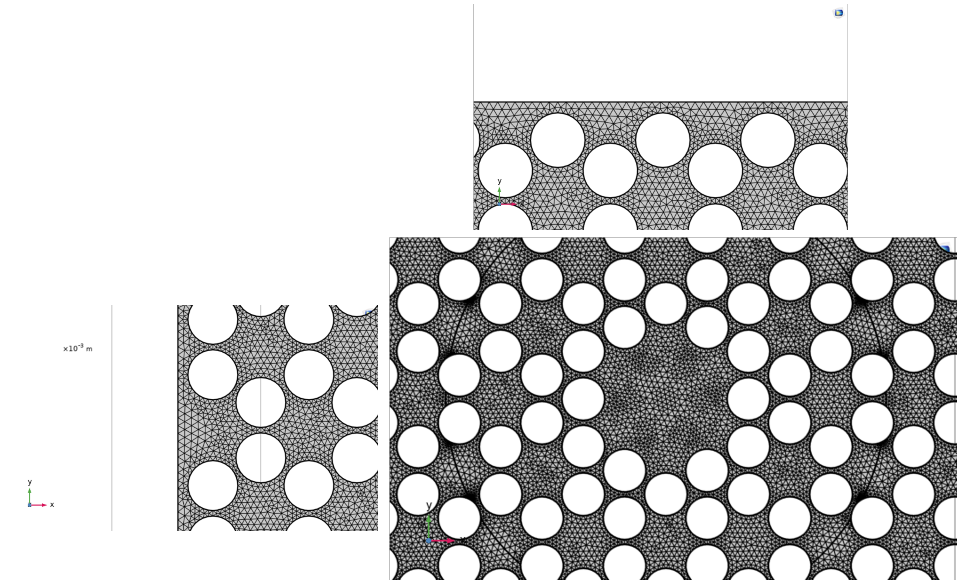

Figure 7: Mesh elements as seen for the small phononic crystal before computing the model.

plot the integral over this surface of the orthogonal displacement. Figure 8 shows this result for the complete range of frequencies found.

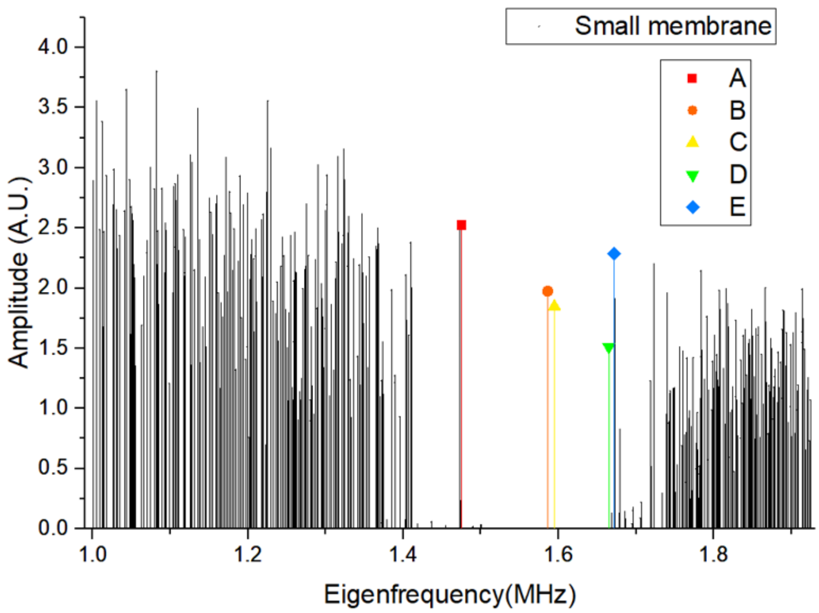


Figure 8: Spectrum of the membrane for the first 600 eigenfrequencies. The labels A-E correspond to the five defect modes found.

It can be seen that in the range of $1.45 <$ frequency $< 1.7\,MHz$ the amount of modes decreases abruptly. This bandgap appears as a consquence of the periodic structure

[23]. Inside this region, five *defect modes* are found, in agreement to the measurements reported by the original paper. Table 4 summarizes these findings. Finally, these modes

| Mode | Measured (MHz) | Simulated (MHz) | Relative (%) |
|---|---|---|---|
| A | 1.4627 | 1.4747 | 0.8 |
| B | 1.5667 | 1.5863 | 1.3 |
| C | 1.5697 | 1.5949 | 1.6 |
| D | 1.6397 | 1.6649 | 1.5 |
| E | 1.6432 | 1.6716 | 1.7 |

Table 4: Eigenfrequencies found in the simulation compared to those reported in [23].

can be visualized by plotting the orthogonal displacement in the surface of the membrane, the results are shown in figure 9.

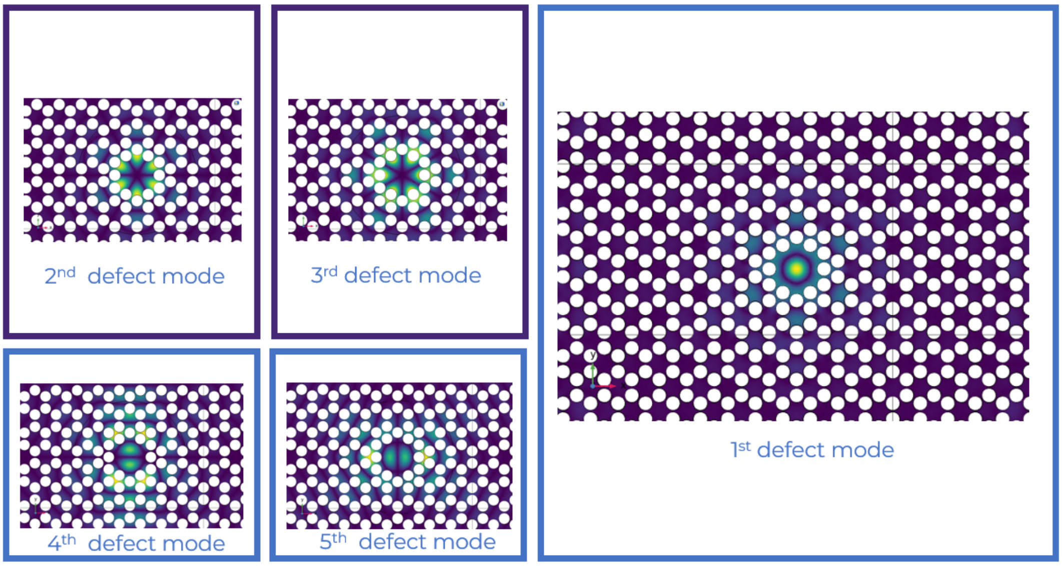


Figure 9: Orthogonal displacement of the membrane for the eigenfrequencies that correspond to defect modes.

From the plots, it can be safely concluded that the modes also feature the same displacement profile as the ones found in [23], thus making sure that no mode was mis-identified during the band gap graph procedure. Another feature found on this figure is the appearence of some modes in frequencies very close to the defect mode eigenfrequencies. These modes will play an important role on the energy loss in the membrane, and are further explored in section 2.2.5

### 2.2.5. Energy loss density

The bending-related energy loss density of the membrane can also be visualized to estimate how the regions of greatest losses have been modified in comparison to the square membrane 2.1. These results are shown in figure 10.

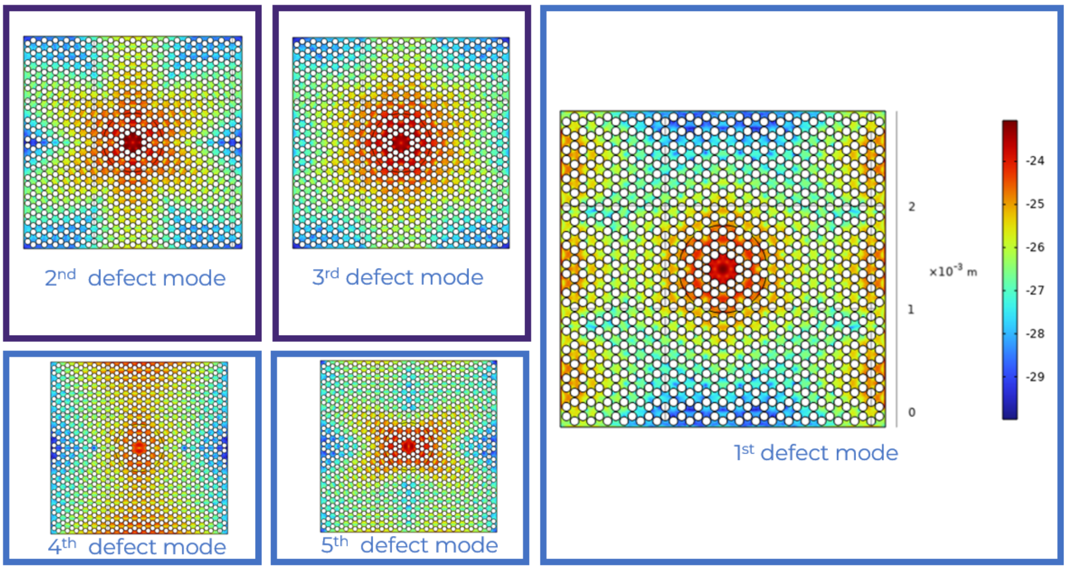


Figure 10: Energy loss density for the phononic crystal.

for comparing bending-related loss of different membranes,the normalized curvature needs to be considered. Figure 11 shows the line graph of normalized curvature for first defect mode in the phononic crystal and the square membrane.

From these plots, it is evident that the semi-periodic membrane suppresses the energy loss at the clamping points of the membrane (the edges). However, a contribution to the energy loss far from the defect is also evident. This contribution could arise from edge modes sufficiently close in frequency to a defect mode. For example, note in figure 8 the close modes (in black) at slightly lower frequencies to the defect mode A (in red). These modes are different by less than 1%, so it is possible in principle that they marginally contribute when the membrane is excited at the defect mode frequency. Figure 12 shows the behaviour of these adjacent eigen-modes, which are also referred to as *edge modes* [25].

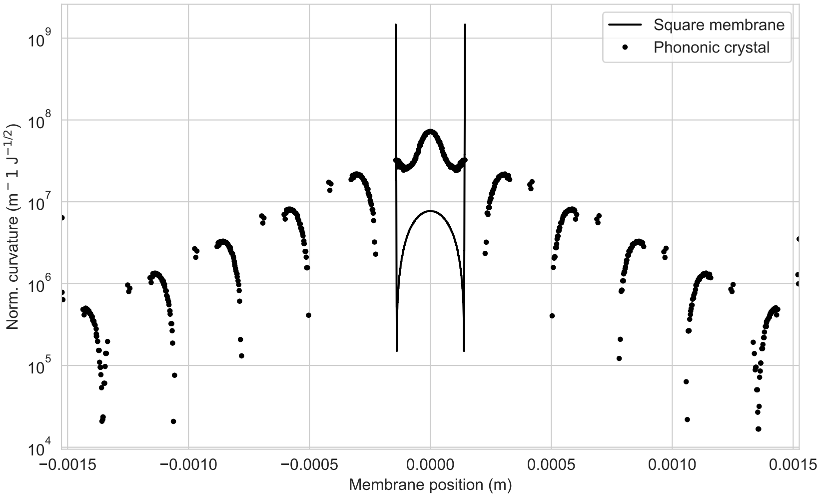


Figure 11: Normalized curvature for both the square membrane and the phononic crystal. It can be seen that higher bending is present in the square membrane, which causes additional energy loss.

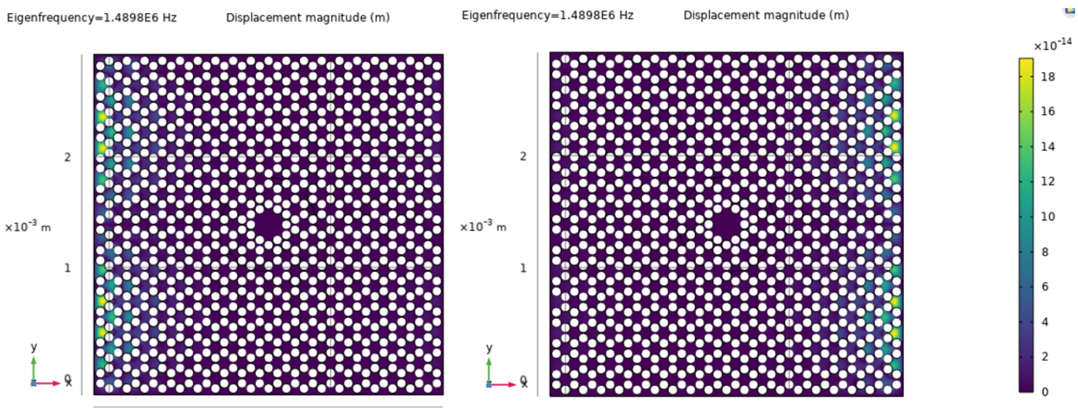


Figure 12: Degenerated edge modes at a close frequency from the fundamental defect mode.

Note that the shape of these edge modes matches the energy density loss pattern seen for the fundamental mode in figure 10. This possible explanation is supported by [25], where the authors suggest that the frame width of the membrane could impact the proximity of the edge modes to the defect ones. These edge modes can contribute in the membrane when it is excited around the defect mode eigenfrequency, which would lower the Q factor ahieved by causing additional energy loss near the edges. Therefore, a natural continuation of the model is a systematic study of the frame width and its impact to the Q factor.

### 2.2.6. Relevance of frame width

A parametric sweep on the frame widths is effectuated to compute the Q factor of similar membranes with different frame widths $fw$ (see Fig. 6). For this systematic study, only the fundamental defect mode was investigated, both for limitations in computer power and time, as well as because it is the most interesting one for our purposes, as due to its symmetry, it couples well to the optical field inside a cavity. Figure 13 shows the calculated Q factor for different frame widths in the fundamental eigen-frequency.

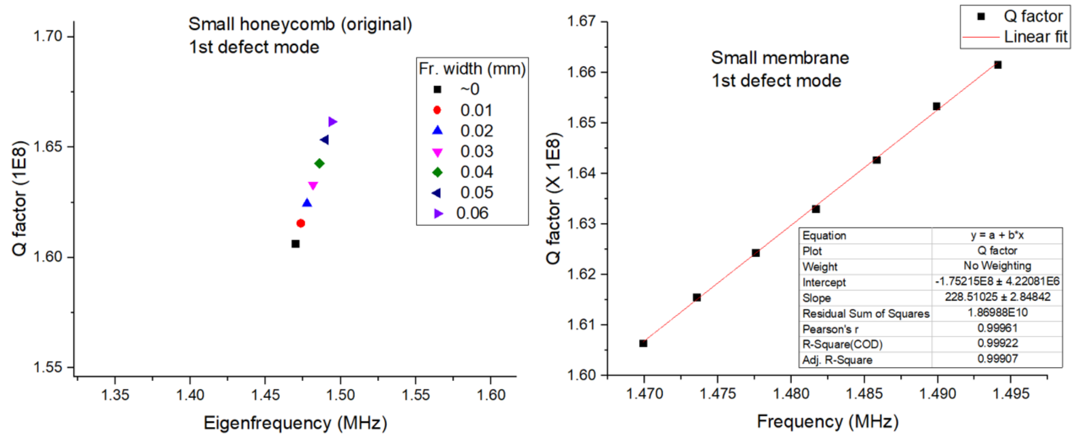


Figure 13: Left: Q factor as a function of the first defect mode eigenfrequency. Right: Strong direct correlation found and parametrized using a linear fit.

From this result, it can be concluded that a wider frame width would help in achieving a larger Q factor. Note however that it also shifts its eigenfrequency to a larger value, so a compromise must be made if the signal of interest has a fixed frequency regime.

The similar direct correlation between Q factor and frame width allows to conclude that the distancing from the defect mode to its neighboring edge modes contributes to achieving a larger Q factor. Furthermore, it is worth remarking that the order of magnitude of the Q factor, regardless of the frame width chosen, is of $10^8$, accordance to the measurements reported in [23].

Even though the behaviour found seems to be highly predictable by a linear trend, figure 14 shows the relation between Q factor and frame width. Here, the bump that appears for a width of around 0.08 mm rrises the question of whether there are Q peaks in the design of the nano-mechanical membrane. If that was the case, a systematic study of these possible features would be suitable if trying to maximize the Q factor around a given vibration frequency.

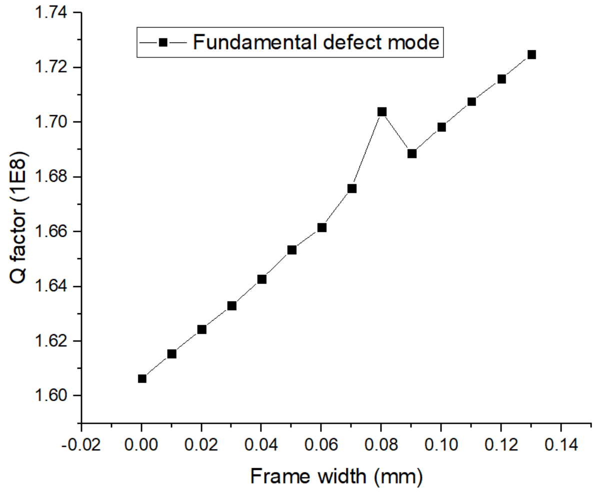


Figure 14: Relation between the Q factor achieved by the phononic crystal and the frame width of the membrane.

Finally, we investigate the decay of the oscillation towards the edges for the fundamental defect mode, to understand how the band gap is supressing the transmision of energy outside the defect. Figure 15 shows the orthogonal amplitude of oscillation at this mode for different frame widths. In all cases, the peak of oscillations happens at the defect, and is strongly damped towards the edges, inidicating that no significant coupling to edge modes occurs.

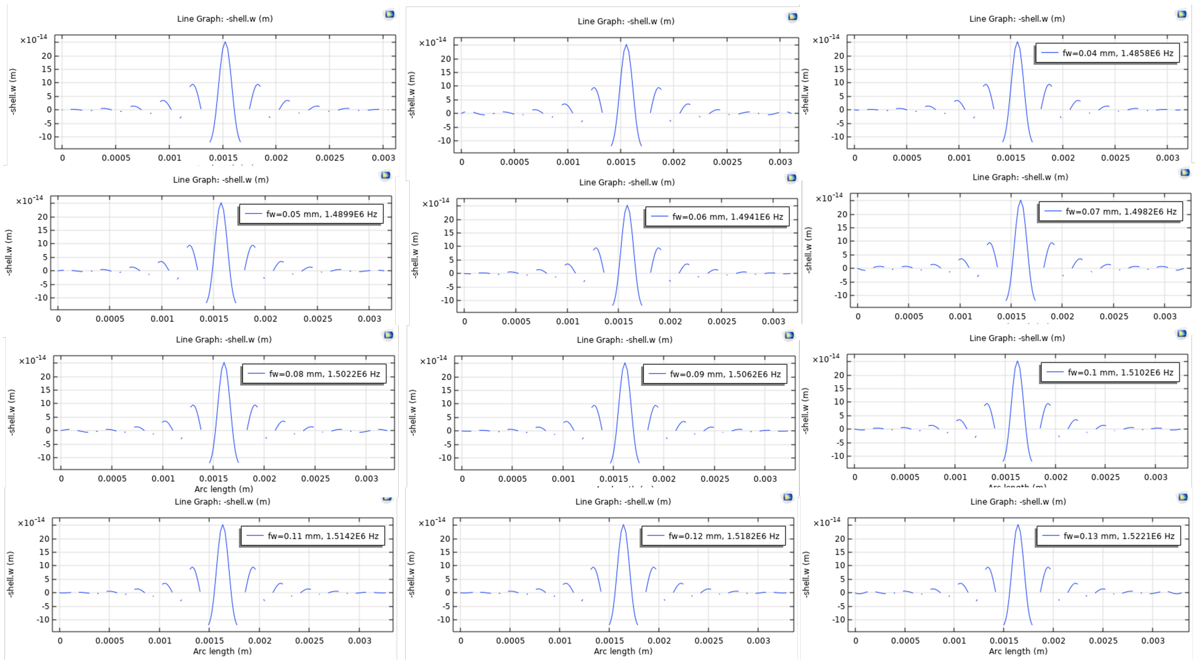


Figure 15: Orthogonal displacement through a vertical line that passes through the center of the membrane for different frame widths. First image of the pannel corresponds to 0 mm frame width and the second one to 0.01 mm.

Note that the behaviour of the oscillation profile does not feature a high dependence on the frame width. At first glance, the curves might appear to be the same, but minor differences can be found looking in detail especially near the edges of the membrane. This observation is consistent with the slight change on Q factor observed when varying the frame width, which in all cases remained in the same order of magnitude.

## 2.3. Scaled phononic crystal

Now, the possibility of improving the Q factor achieved by several orders of magnitude is explored, one way to achieve this is by scaling up the physical size of the membrane. From [23], we infer the scaling to be

$$Q \propto \frac{L^2}{h}, \tag{2.2}$$

where $L$ is the length of the lateral extent of the membrane, and $h$ is the thickness, therefore, for a fixed $h$, a $10\times$ bigger membrane could in theory enhance the Q factor by a factor of 100.

This scaling is still feasible to machine and study in a research-oriented clean room, considering a typical wafer size of 15 cm, devices with lateral extents in the order of few cm can be made. As it is costumary, several of them could still be fit into the wafer, accounting for possible breaking of some of them during the fabrication process without having too much impact on the process efficiency.

Therefore, as an extension of the previous study, a *big membrane* is simulated, keeping $h$ fixed to 35 nm as in the previous case, but increasing its lateral extent by 10 times the original one.

### Membrane geometry

The membrane used corresponds to the same geometry created for the original Phononic crystal studied in section 2.2, it also leaves the material parameters (Poisson ratio, Young modulus, density) unchanged. The parameter with dimensions of longitude (except for the thickness), such as the frame width and the size of the unit cell in terms of the radius of the honeycomb circles a, are rescaled to 10X its previous values. Therefore, it effectively reproduces a membrane of the same material, 10 times bigger in the x-y plane, and with a higher ratio between surface area and thickness.

### Mesh elements

The mesh elements are defined as in table 5. The highlighted parameter "Maximum" needs to be sufficiently small so that a smaller element would not impact the Q factor calculation significantly. For the "small" membrane case, a 60% reduction on this parameter around this number had an impact on the Q factor computation of less than 1%. The elements with dimensions of longitude also correspond to 10 times the values used for the small membrane.

| Max ($\cdot 10^{-6}$ m) | Min ($\cdot 10^{-6}$ m) | Curvature | Res. narrow regions | Max growth rate |
|---|---|---|---|---|
| 51.4 | 1.4 | 0.2 | 1 | Default |

Table 5: Parameters of the customized free triangular mesh

The *big membrane* model was also run in the Maxwell cluster. The time taken to build the mesh was around 12 minutes in the local computer and 9 minutes on Maxwell. In total, the mesh consists of $5.14 \times 10^5$ boundary elements and $4.7 \times 10^4$ edge elements, which lead to a total of $6.4 \times 10^6$ degrees of freedom.

### 2.3.1. Eigenmodes

The model is solved in two setps: First, a membrane of frame width of 0.6 mm is solved by finding the first 600 eigenfrequencies where the defect eigenmodes are for the scaled membrane. Similarly to the analytical square membrane modes, it is found that the eigenfrequencies scale with $f \propto L^{-1}$, with $L$ the lateral size of the membrane. Then, a parametric sweep for different frame widths is computed for 40 eigenmodes around the value of the fundamental defect frequency found in the first step. The second model, which includes the parametric sweep, was solved in Maxwell, needing a total of around

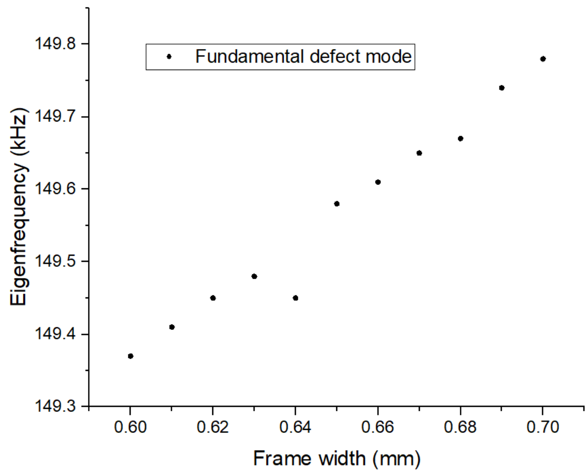


Figure 16: Relation between the fundamental defect mode frequency and the frame width of the membrane. Note that the spacing of the sweep is proportionally smaller than the used in the small membrane

9 hours for 11 different frame widths.

Figure 16 shows the relation between the frequency of the defect mode for different frame widths.

### 2.3.2. Enhancement in Q

The oscillation modes and energy loss density for the big membrane look like those obtained for the small one. However, they key feature is the scaling on the Q factor by $\propto 100$. This was an expected result inferred from [23] here confirmed for several frame widths in numerical simulations. Figure 17 shows the obtained results. It can be seen that regardless of the frame width chosen, the order of magnitude of the Q factor has increased with respect to figure 13.
Moreover, as previously discussed in section 2.2, the parametric sweep on the small membrane suggested the possibility of Q peaks. For the big membrane study, a finer sweep across multiple values around the deviation from the trend shown in figure 16 around $fw = 64\,\text{mm}$ was computed. Figure 17 shows the *raw* data where an evident peak sits at around the mentioned frame width. Here, a linear fit was effectuated to account for the correlation previously displayed in figure 13 between the frame width and the Q factor. The linear trend adjusted to the linear regime shown in the figure reads

$$Q = 0.663[\,\text{mm}^{-1}] \cdot fw + Q_0, \tag{2.3}$$

with

$$Q_0 = 1.6519 \times 10^{10}$$

and $fw$ the frame width measured in mm. This trend is subtracted from the data points,

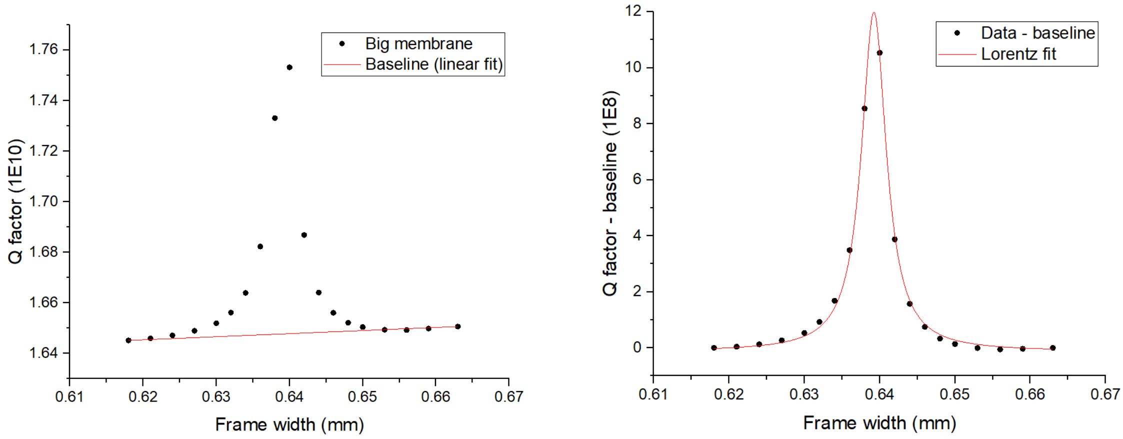


(a) obtained data before baseline subtraction

(b) Fitted Lorentzian peak after a linear trend subtraction

Figure 17: Obtained Q factors for different frame widths in the big membrane

leading to the $Q$ *peak* shown in figure 17b that can be fit with a lorentzian curve of the form

$$Q = \frac{2A}{\pi} \frac{w}{(fw - fw_c)^2 + w^2}. \tag{2.4}$$

The obtained fitting parameters (with $R = 0.998$) are reported in table 6. This result

| Parameter | Value | Description |
|---|---|---|
| $fw_c$ | $(639.23 \pm 0.03)\ \mu$m | central value |
| $w$ | $0.0040 \pm 0.0001$ | FWHM |
| $A$ | $(7.65 \pm 0.16) \times 10^6$ | Area |

Table 6: Parameters used in the Lorentzian fit shown in figure 17b

strongly supports the hypothesis that Q peaks can be found and exploited by fine-tuning the frame width of the membrane resonator. Moreover, the behaviour of the Q peaks was determined with high accuracy, modelled by a Lorentzian distrubution. For the case studied, an optimal choice of $fw$ could enhance the membrane Q factor an additional 10%.

# 3. Cryogenic studies

An implementation of nano-mechanical membranes for high frequency gravitational wave detection also requires the cooling of the membranes inside a low temperature cryostat or cryocooler, which reduces the thermal coupling of the device to the environment.

These systems use liquid helium (which was first time liquefied by Kamerlingh Onnes in 1908) to achieve ultra-low temperatures (below 20 K). But due to the scarce availability of helium in the world, its consumption of it has to be limited and one needs to understand the helium transport inside the cryostat and calculate the amount of helium needed for the operation of the experiment. One of the cooling options, is to use a continous flow liquid helium thermostat [26]. section 3.1 investigates the theoretical background to simulate such a device, which could potentially be used for high energy physics applications.

## 3.1. Theoretical model

A (helium) cryostat contains a fixed volume varying amounts of liquid and gaseous helium. Therefore, the mass flow rates can be described as

$$\begin{aligned} \frac{dm_{\mathrm{L}}}{dt} &= \frac{dm_{\mathrm{L_{in}}}}{dt} - \frac{dm_{\mathrm{boil}}}{dt}, \\ \frac{dm_{\mathrm{G}}}{dt} &= \frac{dm_{\mathrm{boil}}}{dt} - \frac{dm_{\mathrm{G_{out}}}}{dt}. \end{aligned} \tag{3.1}$$

where G and L correspond to the gaseous and liquid components of helium inside of the cryostat, *boil* refers to the boiling liquid helium that is thus converted to gas, *out* referes to the gaseous helium that exits the cryostat through the outlet, and *in* refers to the incoming liquid helium through the inlet.
The internal energy of the helium system can be also decomposed in the liquid and helium parts,

$$E_{total} = m_L u_L + m_G u_G \tag{3.2}$$

where $u$ refers to the internal energy. Given that these quantities are not fixed in time, it is more useful to express this conservation law as a function of time:

$$\frac{de_{total}}{dt} = u_{\mathrm{L}}\frac{dm_{\mathrm{L}}}{dt} + u_{\mathrm{G}}\frac{dm_{\mathrm{G}}}{dt} + m_{\mathrm{L}}\frac{du_{\mathrm{L}}}{dt} + m_{\mathrm{G}}\frac{du_{\mathrm{G}}}{dt}. \tag{3.3}$$

An alternative way to express the total energy is through its legendre transformation between volume and pressure,

$$H = e + pV \tag{3.4}$$

where $H$ is the enthalpy of the system, and $p, V$ the thermodynamic variables of pressure and volume. Deriving both sides with respect to time,

$$\begin{aligned} \frac{de}{dt} &= \frac{dH}{dt} - \frac{d(pV)}{dt} \\ &= \frac{d\left(m_{\mathrm{L}}h_{\mathrm{L}}\right)}{dt} + \frac{d\left(m_{\mathrm{G}}h_{\mathrm{G}}\right)}{dt} - \frac{d(pV)}{dt}. \end{aligned}$$

Where $h$ represents the internal enthalpy. Replacing the blue terms with equations 3.1 and using the product rule for the derivatives the expression becomes

$$\frac{de}{dt} = h_L\frac{dm_{\mathrm{L_{in}}}}{dt} - h_G\frac{dm_{\mathrm{G_{out}}}}{dt} + \frac{dm_{\mathrm{boil}}}{dt}\left(h_{\mathrm{G}} - h_{\mathrm{L}}\right) + \frac{dQ}{dt}, \tag{3.5}$$

with

$$\frac{dQ}{dt} = m_{\mathrm{L_{in}}} \frac{dh_{\mathrm{L}}}{dt} - m_{\mathrm{G_{out}}} \frac{dh_{\mathrm{G}}}{dt} - \frac{d\,(pV)}{dt} \tag{3.6}$$

is identified as the heat flow inside the cryostat. given that both equations 3.3 and 3.5 are equal to the rate of change in the total energy, the terms can be matched, arriving to

$$\begin{aligned} u_{\mathrm{L}} \frac{dm_{\mathrm{L}}}{dt} + u_{\mathrm{G}} \frac{dm_{\mathrm{G}}}{dt} + m_{\mathrm{L}} \frac{du_{\mathrm{L}}}{dt} + m_{\mathrm{G}} \frac{du_{\mathrm{G}}}{dt} = \\ \frac{dm_{\mathrm{L_{in}}}}{dt} - \frac{dm_{\mathrm{G_{out}}}}{dt} + \frac{dm_{\mathrm{boil}}}{dt} \left(h_{\mathrm{G}} - h_{\mathrm{L}}\right) + \frac{dQ}{dt} \end{aligned} \tag{3.7}$$

By using the chain rule, it is possible to identify the term in red as

$$\left( m_{\mathrm{L}} \frac{du_{\mathrm{L}}}{dP} + m_{\mathrm{G}} \frac{du_{\mathrm{G}}}{dP} \right) \frac{dP}{dt} = a_2 \frac{dP}{dt} \tag{3.8}$$

in accordance to [26]. Substituting equation 3.1 into equation 3.7, some terms vanish. The remaining terms read

$$\begin{aligned} a_2 \frac{dP}{dt} = \frac{dQ}{dt} + \frac{dm_{\mathrm{L_{in}}}}{dt} \left(h_{\mathrm{L}} - u_{\mathrm{L}}\right) + \frac{dm_{\mathrm{G_{out}}}}{dt} \left(u_{\mathrm{G}} - h_{\mathrm{G}}\right) \\ + \frac{dm_{\mathrm{boil}}}{dt} \left(h_{\mathrm{G}} - u_{\mathrm{G}} - \left(h_{\mathrm{L}} - u_{\mathrm{L}}\right)\right) \end{aligned} \tag{3.9}$$

and the term in blue can again be identified in accordance to [26] as $a_1$.

Furthermore, consider the total liquid mass in terms of the cross-section of the cryostat $S$ and the density of the liquid helium $\rho_{\mathrm{L}}$,

$$m_{\mathrm{L}} = \rho_{\mathrm{L}} \mathcal{H} S = m_{\mathrm{L_{in}}} - m_{\mathrm{boil}}, \tag{3.10}$$

where $\mathcal{H}$ is the height that the liquid level reaches inside the cryostat. Therefore,

$$\frac{d\mathcal{H}}{dt} = \frac{\frac{dm_{\mathrm{L_{in}}}}{dt} - \frac{dm_{\mathrm{boil}}}{dt}}{\rho_{\mathrm{L}} S}. \tag{3.11}$$

Equations 3.9 and 3.11 determine the evolution of the thermodynamic values of pressure and volume (in terms of the liquid level) of the liquid helium inside the cryostat. These differential equations can be solved numerically using the expression for the internal energy found in [27] based on a linear regression on experimental data.

## 3.2. Numerical model

To solve numerically for the thermodynamic evolution of the liquid helium inside the cryostat, the following initial conditions are chosen:

- **Boiling mass flow rate:** In accordance with [26], this parameter was treated as a constant through the temporal evolution of the system, and was set to $3.95 \times 106{-}3\,\mathrm{kgs}^{-1}$ based on [28].
- **Initial gaseous and liquid helium mass inside the cryostat:** It was assumed that the cryostat was initially empty.
- **Liquid mass flow rate through the inlet of the cryostat:** $4.95 \times 10^{-3}\,\mathrm{kgs}^{-1}$
- **Gaseous mass flow rate through the outlet of the crysotat:** $3.9 \times 10^{-5}\,\mathrm{kgs}^{-1}$
- **Initial pressure and liquid level:** 1.3 Pa and 40.5% respectively.
- **Geometry of the cryostat:** vertical cylinder with radius r = 0.4 m and height $\mathcal{H}_{\max} 0.1\, m$

The system was evolved in an interval of 3000 s with $\Delta t = 50\,\mathrm{s}$. The code created to simulate the system can be found in appendix A. Figure 18 shows the resulting behaviour of pressure and liquid level inside the cryostat as a function of time.

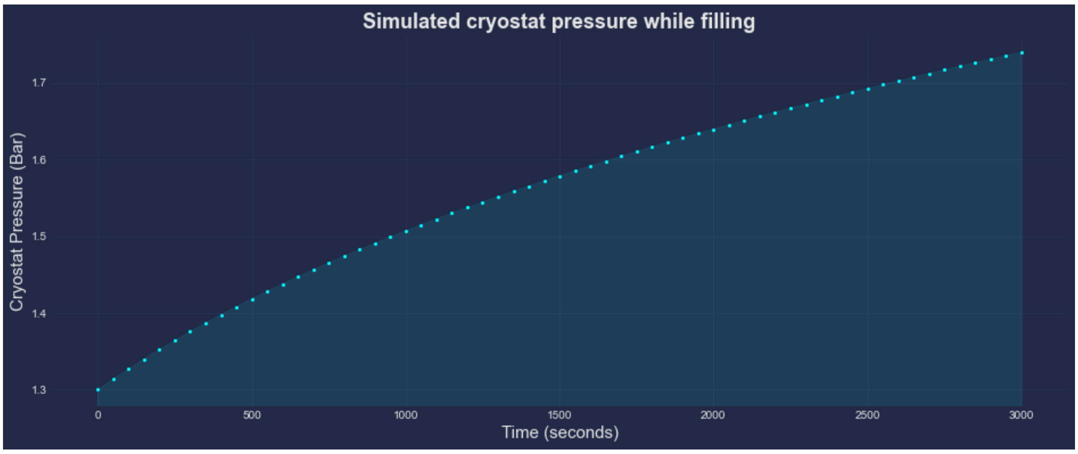


(a) Cryostat pressure as a function of time, as obtained from solving equation 3.3

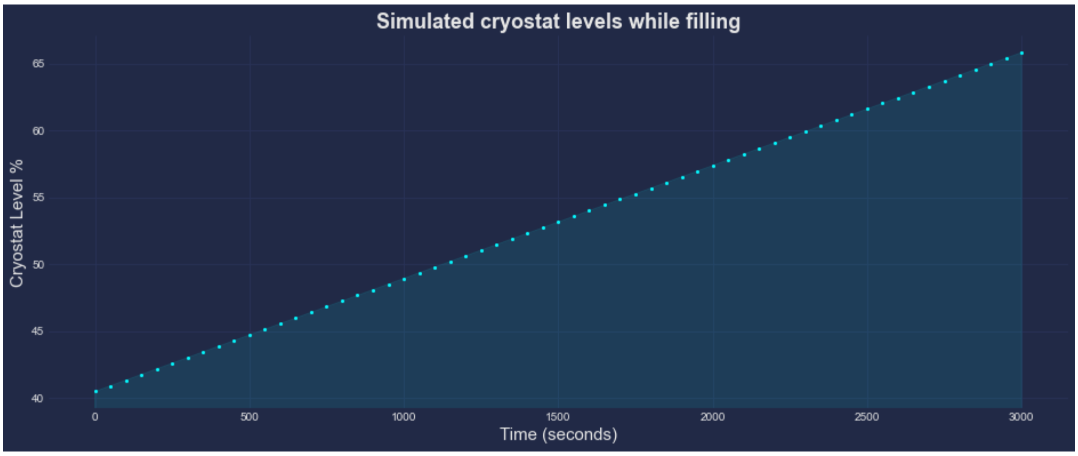


(b) Liquid helium level simulation

Figure 18: Simulated helium behaviour inside a cryostat, obtained after solving numerically equation 3.5

The thermodynamics of the system are in agreement to what is expected if the liquid inlet and gaseous outlet are fixed to a particular value, as long as the incoming liquid mass flow rate is greater than the gaseous outflow. However, the results found disagree with those reported in [26]. This could be caused by a varying inlet mass flow rate that is not reported in the literature found, and which is probably related to the experimental data points measured for a particular application.

# 4. Conclusion

In this project, we implemented a COMSOL model to simulate mechanical resonance frequency and quality factor of a phononic crystal membrane made out of silicon nitride. A comparison of simulated values with measurements reported in literature shows a very good agreement for a mm-scale membrane with resonance frequencies $\sim 1.5\,\mathrm{MHz}$ and quality factors $Q \sim 10^8$. As a first step towards adapting the membrane design for high-frequency gravitational wave detection, I simulated a membrane with a tenfold larger (i.e., cm-scale) lateral extent. The resulting resonance frequencies $\sim 150\,\mathrm{kHz}$ and quality factors $Q \sim 10^{10}$ match the expected linear and quadratic scaling with the lateral extent, respectively.

Moreover, we find that varying the frame width of the membrane can cause *$Q$ peaks* with a measurable impact on the computed Q factor beyond what we could find in the literature, which can be modelled by a Lorentzian distribution. It is not clear why this behaviour emerges and will be a matter of research in the future.

Furthermore, the quality factor can be further increased by cooling the membrane to liquid helium temperatures. As this cooling should not introduce any additional vibrations, we considered operation with a continuous flow cryostat. To estimate the helium consumption, I implemented a corresponding thermodynamical model in Python, which provides a first estimate for the temporal evolution of the thermodynamical variables inside the cryostat.

With regard to further optimizing the membrane geometry, additional systematic variations of its geometry can be investigated. For example, assessing the impact of the hole diameter for the honeycomb lattice or adding additional holes of smaller diameter to the central defect.

# 5. Acknowledgements

This project was developed during the 2022 Summer student program at DESY, Hamburg. In particular, the guidance of Dr. Christoph Reinhardt and Dr. Udai Singh were crucial to bringing this study to a succesful completion.

Also, I would like to thank Dr. Axel Lindner for enabling my visit to DESY, where I also met wonderful people. It was an unforgettable highly enriching experience for me.

This research was supported in part through the Maxwell computational resources operated at Deutsches Elektronen-Synchrotron DESY, Hamburg, Germany.

# References

[1] Anson Hook. Tasi lectures on the strong cp problem and axions. *arXiv preprint arXiv:1812.02669*, 2018.

[2] B Majorovits et al. Madmax: A new road to axion dark matter detection. In *Journal of Physics: Conference Series*, volume 1342, page 012098. IOP Publishing, 2020.

[3] JK Vogel, FT Avignone, G Cantatore, JM Carmona, S Caspi, SA Cetin, FE Christensen, A Dael, T Dafni, M Davenport, et al. Iaxo-the international axion observatory. *arXiv preprint arXiv:1302.3273*, 2013.

[4] Asimina Arvanitaki, Savas Dimopoulos, Sergei Dubovsky, Nemanja Kaloper, and John March-Russell. String axiverse. *Physical Review D*, 81(12):123530, 2010.

[5] BP Abbott, R Abbott, R Adhikari, P Ajith, Bruce Allen, G Allen, RS Amin, SB Anderson, WG Anderson, MA Arain, et al. Ligo: the laser interferometer gravitational-wave observatory. *Reports on Progress in Physics*, 72(7):076901, 2009.

[6] Benjamin P Abbott, Richard Abbott, TD Abbott, MR Abernathy, Fausto Acernese, Kendall Ackley, Carl Adams, Thomas Adams, Paolo Addesso, RX Adhikari, et al. Observation of gravitational waves from a binary black hole merger. *Physical review letters*, 116(6):061102, 2016.

[7] Karsten Danzmann, LISA Study Team, et al. Lisa: laser interferometer space antenna for gravitational wave measurements. *Classical and Quantum Gravity*, 13(11A):A247, 1996.

[8] Michele Maggiore, Chris Van Den Broeck, Nicola Bartolo, Enis Belgacem, Daniele Bertacca, Marie Anne Bizouard, Marica Branchesi, Sebastien Clesse, Stefano Foffa, Juan García-Bellido, et al. Science case for the einstein telescope. *Journal of Cosmology and Astroparticle Physics*, 2020(03):050, 2020.

[9] Nancy Aggarwal, Odylio D Aguiar, Andreas Bauswein, Giancarlo Cella, Sebastian Clesse, Adrian Michael Cruise, Valerie Domcke, Daniel G Figueroa, Andrew Geraci, Maxim Goryachev, et al. Challenges and opportunities of gravitational-wave searches at mhz to ghz frequencies. *Living reviews in relativity*, 24(1):1–74, 2021.

[10] Nancy Aggarwal, George P Winstone, Mae Teo, Masha Baryakhtar, Shane L Larson, Vicky Kalogera, and Andrew A Geraci. Searching for new physics with a levitated-sensor-based gravitational-wave detector. *Physical review letters*, 128(11):111101, 2022.

[11] Asimina Arvanitaki and Andrew A Geraci. Detecting high-frequency gravitational waves with optically levitated sensors. *Physical review letters*, 110(7):071105, 2013.

[12] Asimina Arvanitaki and Andrew A Geraci. Detecting high-frequency gravitational waves with optically levitated sensors. *Physical review letters*, 110(7):071105, 2013.

[13] K.-K. Ni, R. Norte, D. J. Wilson, J. D. Hood, D. E. Chang, O. Painter, and H. J. Kimble. Enhancement of mechanical $q$ factors by optical trapping. *Phys. Rev. Lett.*, 108:214302, May 2012.

[14] Markus Aspelmeyer, Tobias J Kippenberg, and Florian Marquardt. Cavity optomechanics. *Reviews of Modern Physics*, 86(4):1391, 2014.

[15] P-L Yu, TP Purdy, and CA Regal. Control of material damping in high-q membrane microresonators. *Physical review letters*, 108(8):083603, 2012.

[16] S Chakram, YS Patil, L Chang, and M Vengalattore. Dissipation in ultrahigh quality factor sin membrane resonators. *Physical review letters*, 112(12):127201, 2014.

[17] Mohammad J Bereyhi, Amirali Arabmoheghi, Alberto Beccari, Sergey A Fedorov, Guanhao Huang, Tobias J Kippenberg, and Nils J Engelsen. Perimeter modes of nanomechanical resonators exhibit quality factors exceeding 10 9 at room temperature. *Physical Review X*, 12(2):021036, 2022.

[18] COMSOL AB, Stockholm, Sweden. Comsol multiphysics®. https://www.comsol.com, 2022. v. 5.3.

[19] P-L Yu, TP Purdy, and CA Regal. Control of material damping in high-q membrane microresonators. *Physical review letters*, 108(8):083603, 2012.

[20] Luis Guillermo Villanueva and Silvan Schmid. Evidence of surface loss as ubiquitous limiting damping mechanism in sin micro-and nanomechanical resonators. *Physical review letters*, 113(22):227201, 2014.

[21] P-L Yu, TP Purdy, and CA Regal. Control of material damping in high-q membrane microresonators. *Physical review letters*, 108(8):083603, 2012.

[22] Christoph Reinhardt, Tina Müller, Alexandre Bourassa, and Jack C Sankey. Ultralow-noise sin trampoline resonators for sensing and optomechanics. *Physical Review X*, 6(2):021001, 2016.

[23] Yeghishe Tsaturyan, Andreas Barg, Eugene S Polzik, and Albert Schliesser. Ultracoherent nanomechanical resonators via soft clamping and dissipation dilution. *Nature nanotechnology*, 12(8):776–783, 2017.

[24] Dennis Høj, Fengwen Wang, Wenjun Gao, Ulrich Busk Hoff, Ole Sigmund, and Ulrik Lund Andersen. Ultra-coherent nanomechanical resonators based on inverse design. *Nature communications*, 12(1):1–8, 2021.

[25] E Ivanov, T Capelle, M Rosticher, J Palomo, T Briant, P-F Cohadon, A Heidmann, T Jacqmin, and S Deléglise. Edge mode engineering for optimal ultracoherent silicon nitride membranes. *Applied Physics Letters*, 117(25):254102, 2020.

[26] Rundong Yan and Ziyun Jiang. Thermodynamic modeling of continuous flow liquid helium thermostat. In *Journal of Physics: Conference Series*, volume 2012, page 012005. IOP Publishing, 2021.

[27] Christopher N Regier. Dynamic modeling of a cryogenic system at the canadian light source. 2009.

[28] Shufeng Jin, Shuping Chen, Rongzhen Zhao, Junhui Zhang, and Hailin Su. Thermal structure optimization of a supercondcuting cavity vertical test cryostat. *Cryogenics*, 104:102992, 2019.

# Appendices

## A. Cyogenics code

```python
#Python code, done by Juan PA Maldonado
import numpy as np
import matplotlib.pyplot as plt
from scipy.integrate import odeint as scp_int
import seaborn as sns
sns.set_style("whitegrid")


#Initial parameters for the calculations
rho = 119 #kg/m3. Density of liquid helium at 4.5K
r = 0.8/2 #m. Radius of thermostat
S = 2*np.pi*(r**2) #m^2. Bottom area of surface
P_0 = 1.3 #Pa. Initial pressure inside thermostat
max_height = 0.1 #m
h_0 = max_height*0.405 #m. 40.5% of the total level.

delta_t = 50 #s
t_initial = 0#s
t_final = 3000#s
t = np.arange(t_initial,t_final+delta_t,delta_t)#s. simulation time

mG0 = 0 #kg. Assume no initial evaporated helium
mL0 = 1e-3 #kg.
dm_Gout_dt = 3.9e-5 #gaseous outlet flow
dm_Lin_dt = 4.95e-3 # liquid inlet flow.
dm_boil_dt = 3.95e-3 #kg/s. Gas outlet flow.


def u(P,gas_bool=False):
    """
    Internal energy for the liquid helium, values obtained in page 5 of the
        paper.
    Expression valid in the P \in 0.9-1.5 bar range.

    """
    if gas_bool==True:
        lambda_u = -1.9034e-7
        gamma_u = 0.03977
        eta_u = 12638.58
    else:
        lambda_u = 0
```

```
        gamma_u = 0.04897
        eta_u = -5794.82

    return lambda_u*(P**2) + gamma_u*P + eta_u

#deriving with respect to time:
def du_L_dP_func(P):
    lambda_u = 0
    gamma_u = 0.04897
    return lambda_u*(P) + gamma_u
def du_G_dP_func(P):
    lambda_u = -1.9034e-7
    gamma_u = 0.03977
    return lambda_u*(P) + gamma_u

def enthalpy(u,P,rho):
    """
    internal enthalpy of the liquid helium
    """
    return u + (P/rho)

#dynamic mathematical models of LIQUID LEVEL (h) and PRESSURE (P)

def dm_L_dt(dm_Lin_dt,dm_boil_dt):
    return dm_Lin_dt - dm_boil_dt

def dm_G_dt(dm_boil_dt,dm_Gout_dt):
    return dm_boil_dt - dm_Gout_dt

def a1_func(dm_Lin_dt,hL,uL,dm_Gout_dt,uG,hG):
    """
    a1 parameter
    """
    return dm_Lin_dt*(hL-uL) +dm_Gout_dt*(uG-hG)

def a2_func(mL,du_L_dP,mG,du_G_dP):
    """
    a2 parameter
    """
    return mL*du_L_dP + mG*du_G_dP


def dPdt(P,t,dm_boil_dt,dm_Lin_dt,dm_Gout_dt,mL0,mG0):
    """
    Differential equation describing the change of pressure as a function of
        time
```

```
    """
    uL = u(P)
    uG = u(P,gas_bool=True)

    hL = enthalpy(uL,P,rho)
    hG = enthalpy(uG,P,rho)

    a1 = a1_func(dm_Lin_dt,hL,uL,dm_Gout_dt,uG,hG)

    du_L_dP = du_L_dP_func(P)
    du_G_dP = du_G_dP_func(P)

    mL = dm_L_dt(dm_Lin_dt,dm_boil_dt)*t + mL0
    mG = dm_G_dt(dm_boil_dt,dm_Gout_dt)*t + mG0
    heat_term = (du_L_dP + du_G_dP) + S*max_height #Q = U -int(VdP) for fixed
        volume, -> dQdt = (dudP + V)dPdt
    a2 = a2_func(mL,du_L_dP,mG,du_G_dP) + heat_term

    return (a1/a2) + (dm_boil_dt*(hG-hL+uL-uG))/a2

def dhdt(h,t,dm_Lin_dt,dm_boil_dt,rho,S):
    """
    Differential equation describing the change of liquid level as a function
        of time
    rho = density of liquid, S= bottom surface of thermostat
    """
    return (dm_Lin_dt - dm_boil_dt)/rho*S

    Height = scp_int(dhdt,h_0,t,args=(dm_Lin_dt,dm_boil_dt,rho,S))
Pressure = scp_int(dPdt,P_0,t,args=(dm_boil_dt,dm_Lin_dt,dm_Gout_dt,mL0,mG0))

plt.figure(figsize=(16,6))
plt.plot(t,Pressure,marker='o',linestyle='None',markersize=2)
plt.title('Simulated cryostat pressure while
    filling',fontsize=18,fontweight='bold')
plt.xlabel('Time (seconds)',fontsize=15)
plt.ylabel('Cryostat Pressure (Bar)',fontsize=15)
plt.show()

plt.figure(figsize=(16,6))
plt.plot(t,100*Height/max_height,marker='o',linestyle='None',markersize=2)
plt.title('Simulated cryostat levels while
    filling',fontsize=18,fontweight='bold')
plt.xlabel('Time (seconds)',fontsize=15)
plt.ylabel('Cryostat Level %',fontsize=15)
plt.show()
```